Surface Displacement of the May 17, 1993 Eureka Valley, California, Earthquake Observed by SAR Interferometry

by

Gilles Peltzer and Paul Rosen

Jet Propulsion Laboratory
California Institute of Technology
Pasadena, CA **91109,** *USA.*

For Science Magazine

once the variation induced by the reference geoid is removed, is proportional to the local topography (Fig.2A). The phase in a coseismic interferogram (Fig. 2B) spanning the seismic event and processed in the same way is the sum of two terms: one, proportional to the topography and one, to the displacement of the surface related to the earthquake. The phase in the coseismic interferogram is more sensitive to surface displacements than to the topography by several orders of magnitude (3), so centimeter-level displacements contribute substantially to the interferometric fringes in Fig. 2B (11). The topographic signal can be removed from the coseismic interferogram by scaled difference with the preseismic interferogram (12). The resulting interferogram depicts surface displacements related to the earthquake and aftershocks in a direction parallel to the line of sight to the satellite (Fig. 2C) (13).

The ring-shaped fringes in the epicentral area of this interferogram (Fig. 2C) depict subsidence of the surface of the hanging wall in response to the fault slip at depth. The subsidence basin is -35 km in length and -20 km in width, and is oriented slightly west of north. The fringes appear narrower along the south-cast side of the basin than along the west side of it, consistent with displacement produced by a west-dipping fault.

A few residual fringes are visible around the depression and in the far field where surface displacements related to the earthquake are unlikely. Most of these fringes are not topographic residuals because they do not coincide with any features in the preseismic interferogram. The fringes may reflect small surface changes related to water content in the soil or wave propagation delays through the ionosphere and the troposphere (14).

The northern (AA') and central (B B') parts of the subsidence basin are relatively symmetric. This probably results from the great depth to the top of the rupture along these sections of the fault, Some of the surface fractures observed in the Eureka Valley fill basin (arrow A 1 in Fig. 1,3) showed 5 to 20 mm of vertical separation (7). Such offsets are not depicted in the radar measurements even though the noise in the radar data does not exceed a few millimeters in this area (profile AA', Fig. 3). A possible explanation is that the

fractures were shallow and produced displacements attenuated over a short distance from the surface break. In the averaged radar data, the pixel separation is -80 m, and local, vertical separation of the ground across a small surface break may be undetected. Such fractures could have been generated by shallow aftershocks. Because they lie in the center of the depression, and not along its eastern edge, however, it is clear that they do not correspond to the main rupture.

The maximum displacement in the center of the depression is 3.1 cycles of phase, or 8.75 cm in range, corresponding to a vertical displacement of 9.S cm (15). The eastern side of profile BB' shows a gentle bump, higher than the western side, as a result of the slight uplift of the footwall in response to the down-dip slip on the west dipping fault.

Along the eastern edge of the southern part of the basin, profile CC' shows a step of 3 cm. The step can be followed for several kilometers in the interferogrrn, becoming gradually smoother to the north and south. We interpret this feature as a shallow dislocation along the southern section of the fault and a surface break along a small section of it (16). Here the rupture is along a -100 m high escarpment in volcanic deposits in the southern Saline Range. The sharpest phase offset is where the escarpment steps 500 m to the right (Arrow A2 in Fig. 1, 3).

We have conducted a field survey along the fault in order to verify our interpretation. At the base of smaller, -10 m high, N35-45°E escarpments, connecting the two main escarpments, we found evidence of down-to-the-west, displacement of the ground of 1-3 cm. The surface breaks could be followed for a few tens of meters along one escarpment, and formed en echelons steps between the two major fault scarps. The roughness of the basalt in this area prevented us fron ı making a clear map of the rupture. However, the combination of the radar data and the field observations suggests that the main dislocation reached the surface along the southern segment of the fault. That the surface break is observed along the eastern edge of the subsidence basin is in agreement with a westward dip of the main fault plane at depth.

The main shock fault plane strikes north-northeast (4), whereas the axis of the subsidence basin and the aftershock distribution are both oriented 5 to 10“ west of north (Fig. 1, 2C). This pattern suggests that the slip on the fault plane was along, or below a line plunging to the north. Such slip would produce a subsidence basin with a long axis parallel to the trend of the line of maximum slip on the fault plane, rather than to the fault strike direction. If we define this line on a fault plane with clip angle α by the angle δ it makes with the horizontal (Fig. 4), its trend makes an angle $\beta = \tan^{-1}(\cos\alpha \tan\delta)$ with the fault plane strike. An angle β of 15-20°, such as that observed in the data, could be obtained with δ = 22-29” and a fault plane dipping 50’. The hypocenter of the main shock is at a depth of 13 km, in the northwestern part of the subsidence basin, and the surface rupture is along the southeastern edge of the basin. The rupture thus likely propagated upward and southward on a west dipping fault plane.

We modeled the earthquake dislocation as a 15 km long, 16 km wide fault plane striking N7”E and dipping 50” to the west. The plane was divided into 16 patches and maximum slip was assumed to be distributed near the north plunging diagonal of the fault. We imposed the slip to be 3 cm at the surface in the south and no slip on patches located above the zone of maximum slip on the fault plane. The slip values in the lower fault patches were adjusted to match the seismic moment of the earthquake (4). An elastic half space dislocation model (17) shows that such fault parameters imply a subsidence basin with a long axis oriented slightly west of north, consistent with the radar observations. The predicted displacement along profiles BB’ and CC’ is *in* good agreement with the displacement observed with the radar (Fig. 3). Along profile AA’, however, the model predicts a smoother and shallower depression than that observed with the radar. The steep lateral slopes of the observed depression there suggest that shallow sources, such as aftershocks, may have contributed to the subsidence, One of the largest aftershocks actually

occurred at shallow depth in this area two days after the main event (18) (Fig. 1). The effect of this aftershock, which had a steep, west-dipping fault, could also explain the angular shape of the interferometric fringe, just north of AA' (Fig. 2C). The difference between modeled and observed displacements along AA' could also be explained by heterogeneities in sediments along the edges of the basin, such as basement scarps connecting with the large surface scarps in the Saline Range.

We have shown that radar interferometry can provide quantitative results about the mechanism of an earthquake even in remote areas where surface ruptures are not apparent. In a region like the Los Angeles basin, where most faults are blind and earthquakes general] y not associated with surface breaks, radar interferometric maps of coseismic displacement would enhance the resolution offered by conventional geodetic techniques and would help determine the geometry of faults at depth.

References and notes:

1. For example, C. Tsuboi, Bull. Earthquake Res. Inst., Tokyo Univ., 10, 411 (1933).

2. D. Massonnet et al., Nature, 364, 138 (1993).

3. H.A. Zebker, P.A. Rosen, R.M. Goldstein, A.G. Gabriel, C. L. Werner, J. Geophys. Res., 99, 19,617 (1994).

4. The Caltech TERRAscope solution is: strike= -172.9", dip = 47.7" to the west, rake = -109", depth = 13 km, and moment = 1.6 10^{18} Nm, and the Harvard CMT solution is strike = 218", dip = 39", rake = -80", depth = 15 km, and moment = 1.2 10^{18} Nm. Both mechanisms indicate normal faulting with a mostly down dip motion and a small right lateral-component.

5. The region comprised between Owens Valley and Death Valley is characterized by northwest-southeast extension expressed at the surface in a series of north-northeast, prominent normal faults, including the Deep Spring fault, the fault bounding the narrow valley east of the Saline Range, and the fault west of the Cottonwood mountains (Fig. 1). Within the Saline Range, the deformation is distributed over several smaller faults connecting with Saline Valley across late Cenozoic volcanic deposits. The morphology of these faults, both in the field and *on* satellite imagery, and geodetic measurements suggest recent activity [W.A. Bryant, California Geol., 42 (1989); M. Rehis, in M. Lahren, J. Trexler and C. Spinisa, eds., Crustal Evolution of the Great Basin and Sierra Nevada, Field Trip Guide, Univ. of Nevada, Reno (1993);); J. Il. Minster and T.H. Jordan, J. Geophys. Res., 92, 4798 (1987); T.H. Dixon, S. Robaudo, J. Lee, Tectonics, in press].

6. In the week following the earthquake, a portable seismic network was deployed in the Eureka Valley by seismologists from the University of Reno, Nevada. J. Louie, personal communication.

7. The ground ruptures were observed along the base of two west-facing scarps emanating from the Saline Range and extend northward into the valley over a distance of 3-4 km.

They consist of left-stepping echelons, generally open fissures, some of them showing a vertical separation of 5-20 mm, down to the west, consistent with the cumulative displacement expressed in the scarps topography [Suzanne Hecker, unpublished data].

8. ERS-1 SAR data were acquired on 14 Sep 1992, 23 Nov 1992, and 8 Nov 1993. Raw SAR data were processed directly to interferograms (10).

9. A.G. Gabriel, R.M. Goldstein, and H.A. Zebker, J. Geophys. Res., 94,9,183 (1989).

10. In each SAR image pixel, the phase value represents a measure modulo-2π of the distance between the radar antenna and the ground. An interferogram is obtained by averaging the product of one complex SAR image and the complex conjugate of another image, after sub-pixel coregistration (3), The phase. of each pixel in an interferogram is the difference of the phase of the corresponding pixels in the two SAR images.

11. The interferometric baseline is the distance between the two orbits from which the data were acquired. In an intetferogram, the ambiguity height is defined as the topographic elevation difference that would produce a phase variation of 2π and is inversely proportional to the component of the baseline perpendicular to the satellite line of sight. In the coseismic interferogram, the ambiguity height is about 78 m and varies by 7% across the scene. On the other hand, the line of sight surface displacement which would produce a phase variation of 2π is 28 mm (half the radar wavelength), independent of the imaging geometry. Therefore, the sensitivity to surface displacement is about 2785 times greater than to elevation variations.

12. Differencing the phase of two interferograms requires one phase field to be scaled to the same fringe rate as the other (3), so at least one phase field must be unwrapped [R.M. Goldstein, H.A. Zebker and C.L. Werner, Radio Sci., 23, 713 (1988)]. The ability to unwrap the phase depends on the noise level in the system and the fringe rates in the image. Because the coseismic interferogram in Fig 2B has a smaller fringe rate than that in Fig, 2A, we unwrapped the coseismic phase, scaled it to the intrinsic fringe

rate of the preseismic interferogram, and computed their difference. We then unwrapped the resulting interferogram, which has many fewer fringes, and scaled the phase back to the coseismic rate (Fig. 2C).

13. For ERS-1, the satellite line of sight is nearly perpendicular to the orbit and has an incidence angle of 23° in the center of the scene [European Space Agency, ERS-1 System, 87 pp., ESA Publi. Div., ESTEC, Noordwijk, The Netherlands (1992)].

14. Atmospheric phase propagation delays estimated for L-band microwaves by the Global Positioning System can reach about two meters through the ionospheric and tropospheric layers [D.M. Tralli and S.M. Lichten, Bull. Geod., 64, 127 (1990)]. SAR interferograms probably depict variations of this signal across a scene but the distinction from effects due to other sources are unclear [D. Massonnet and K. Feigl, EOS Trans. AGU, '75, suppl. (1994)].

15, In the middle of the depression, the displacement of the ground is essentially vertical, so its magnitude is given by the observed value of the range displacement divided by the cosine of the incidence angle (1 3).

16. A phase offset of 2.8 cm could arise from a phase unwrapping error, which is most likely to occur in regions of sharp topography such as that of the Saline Range. However, when following a close contour, a phase unwrapping error must be balanced by a phase offset of opposite sign. The fact that it is possible to connect both ends of profile CC' following a smooth phase contour running around the zone of phase discontinuity allows us to rule out this hypothesis.

17. Y. Okada, Bull. Seism. Sot. Am., 75, 1135 (1985).

18. The aftershock sequence includes four events of M>4.5 (Fig. 1). One of them occurred near the northeast part of the subsidence basin and has the following parameters: strike = -179.3°, dip = 74° to the west, rake = -101°, depth = 5 km, and moment = 1.23 10^{16} Nm (19).

19. H. K. Thio, personal communication.

20. We thank S. Hecker for providing an unpublished surface rupture map, J. Louie for providing relocated aftershock coordinates, R. Annijo for participation in field work, and E. Ivins and K. Hudnut for critically reading the first version of the manuscript. ERS-1 data were provided by ESA. The work was performed at the Jet Propulsion Laboratory under contract with NASA.

Figure captions:

Fig. 1: Active fault map of the Eureka Valley region over a shaded USGS topographic map. Faults are from interpretation of Landsat TM image. White contour depicts projected fault plane as modeled in this study. Light shaded area in fault plane is zone of non-zero slip, Arrow A 1 shows location of surface breaks recognized in the field after the earthquake (7). Arrow A2 points to fault segment where seismic rupture reached the surface, as inferred from the radar data. Dashed line delineates area shown in Fig. 2. Large star indicates location of main shock, small stars, locations of aftershocks of magnitude greater than 4.5, and circles smaller aftershocks (6). Focal mechanism of the main shock is depicted (19).

Fig. 2: SAR interferograms formed from combination of the 14 Sep. 1992-23 Nov. 1992 (A), and the 23 Nov. 1992-8 Nov. 1993 (B) SAR images, and by double difference (C) of interferograms in (A) and (B). Black areas in (B) and (C) are zones of low coherence that have been masked before unwrapping the phase (12). They correspond to zones of major surface changes such as over sand dunes or cultivated fields, and to zones of phase ambiguities produced by overlays on steep slopes facing toward the satellite. Black masks are absent in interferogram (A) because it has not been unwrapped, The phase value is color coded and laid over the radar intensity image for reference. The interferometric baseline (11) of the second image pair (B) being smaller than that of the first pair (A), the fringe spacing is larger in the map of Fig. 2A than it is in the map of Fig. 2B. In (A), a full color cycle corresponds to an elevation difference of 50 m. In (B), a full color cycle can be due to either an elevation difference of 78 m, 28 mm of line of sight surface displacement (half the radar wavelength), or a combination of the two. In the 3-pass interferogram (C), where the topography has been removed, a full color cycle corresponds to a displacement

of the ground of 28 mm in the direction of the satellite. White lines in (C) indicate location of profiles shown in Fig. 3.

Fig. 3: Profiles of surface displacement observed with the radar (solid lines) and predicted with an elastic dislocation model (dashed lines) (17). Profiles are corrected for the geometric distortion induced by topography in radar imagery. Arrow Al in profile AA' indicates location where surface cracks were observed (7). Arrow A2 in profile CC' points to the place where the main rupture reached the surface.

Fig. 4: Sketch showing a plunging slip distribution on a fault plane with dip angle α.

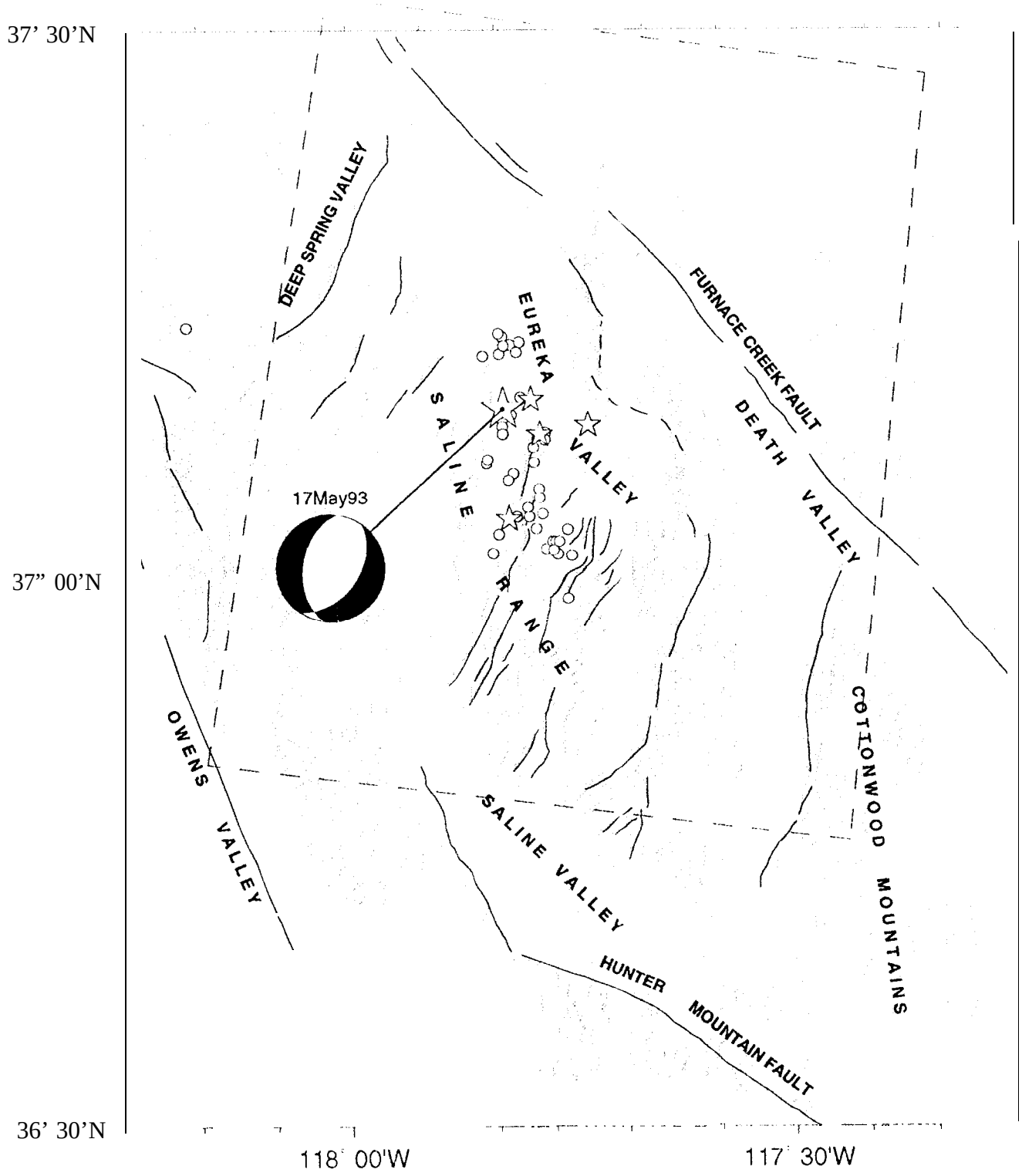
37’ 30’N
37” 00’N
36’ 30’N
118° 00'W
117° 30'W
DEEP SPRING VALLEY
EUREKA
VALLEY
SALINE
RANGE
17May93
FURNACE CREEK FAULT
DEATH
VALLEY
COTTONWOOD
MOUNTAINS
OWENS
VALLEY
SALINE VALLEY
HUNTER
MOUNTAIN FAULT

Figure 1

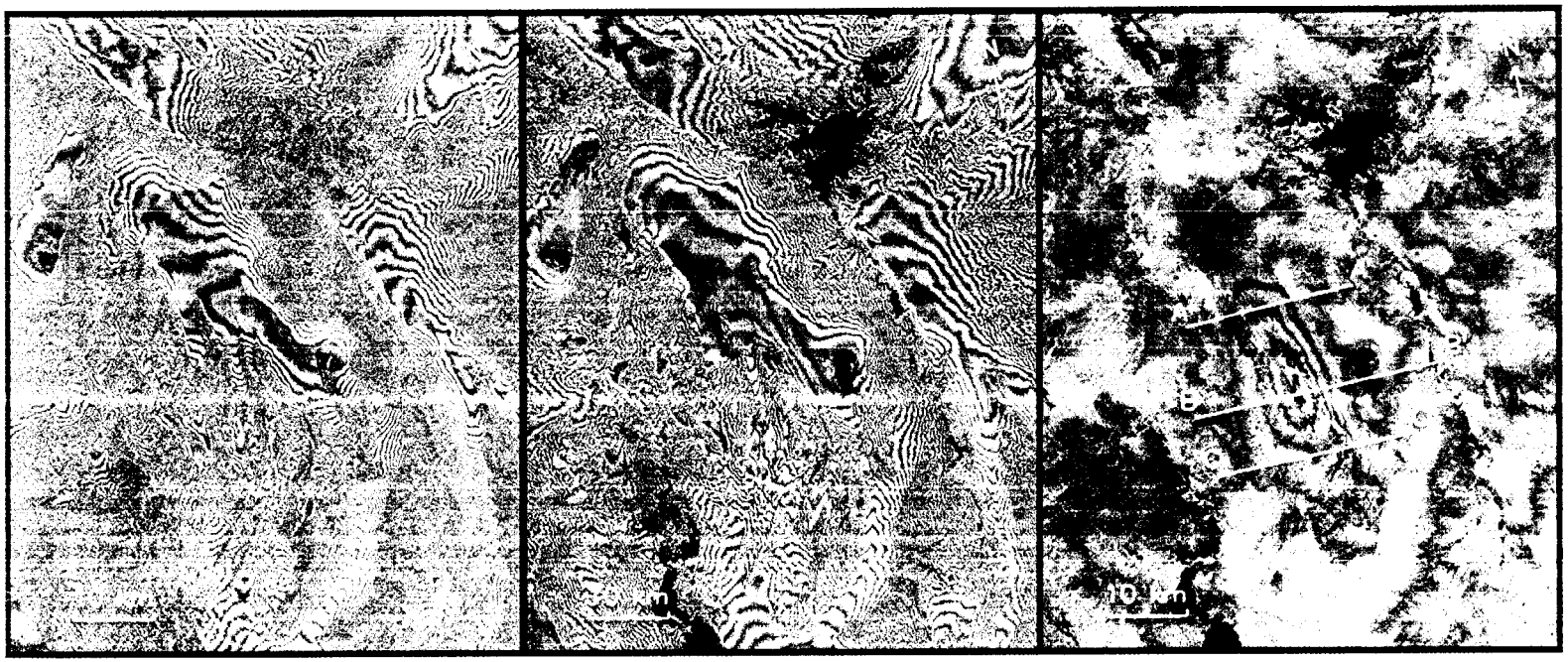

Figure 2

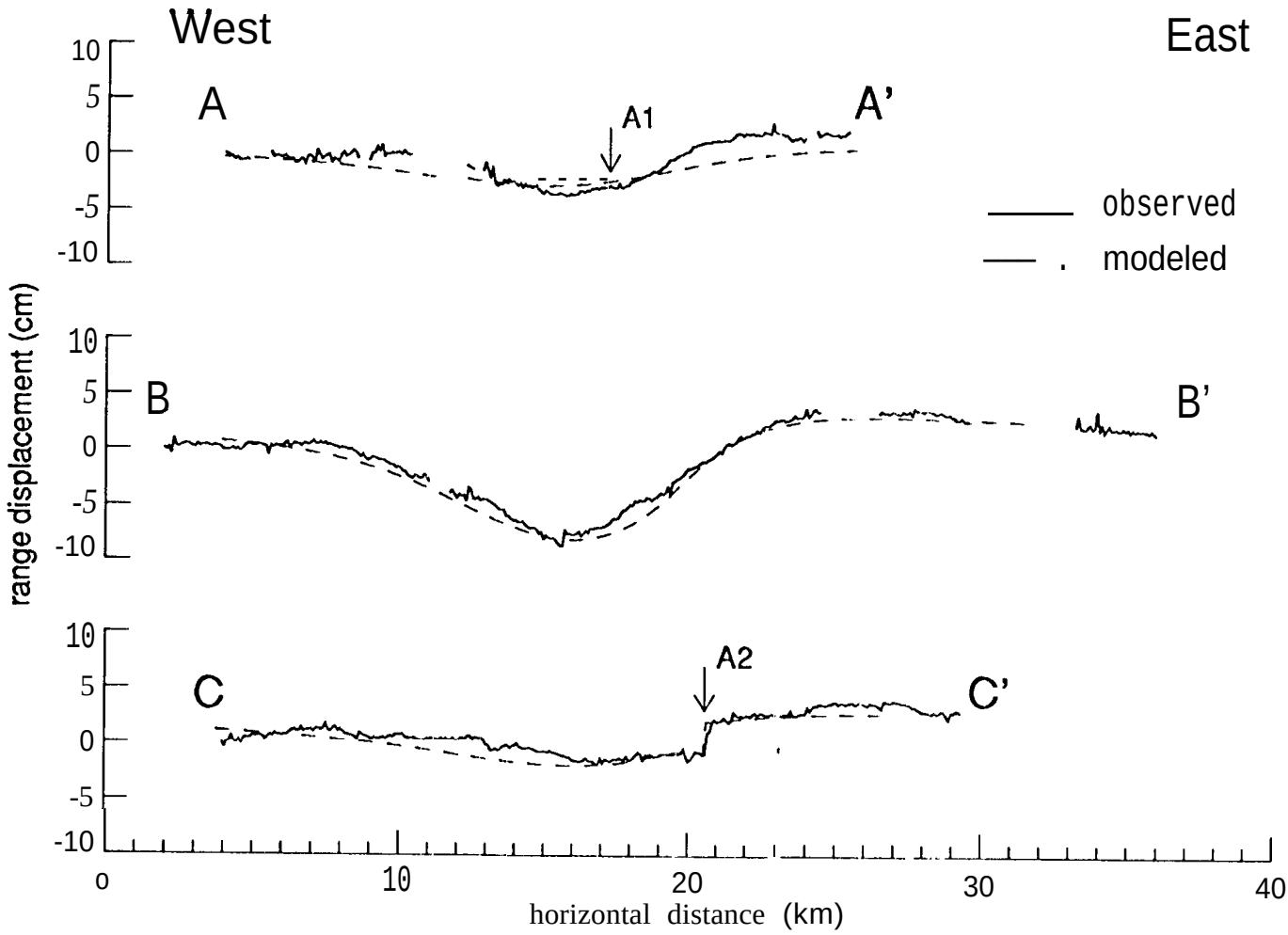
West
East
A
A'
A1
B
B'
C
C'
A2
observed
modeled
range displacement (cm)
horizontal distance (km)
10
5
0
-5
-10
0
10
20
30
40

Figure 3

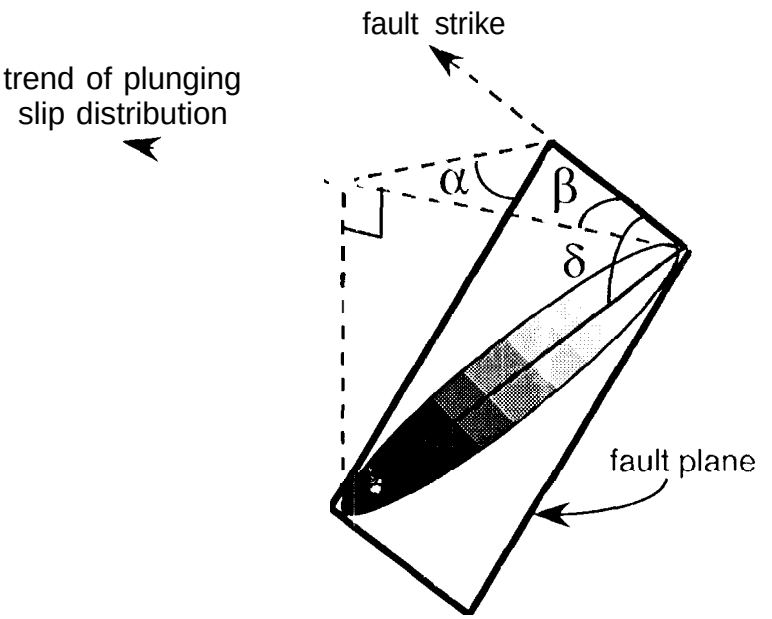
fault strike
trend of plunging
slip distribution
α
β
δ
fault plane

Figure 4